UCB-NE-4233

Analysis of Expanding Bentonite

Kazuyuki Shinoda, Paul L. Chambré, and Joonhong Ahn

Department of Nuclear Engineering
University of California, Berkeley
Berkeley, California 94720-1730

March 2001

The authors invite comments and would appreciate
being notified of any errors in the report

Paul L. Chambré
Department of Nuclear Engineering
University of California
Berkeley, CA 94720-1730
USA

cham@newton.berkeley.edu

Table of Contents

List of Figures

List of Tables

1. Introduction

1.1 Background

In the geologic disposal of high-level radioactive waste, which is currently under investigation in most countries operating nuclear facilities, the waste is buried in a geologic formation at more than several hundred meters underground using some engineered barriers such as a waste container and a buffer material. The space between the host rock and the waste container is filled with the buffer material. The main functions of the buffer material are (a) to retard the groundwater flow between the host rock and the waste container; and (b) once radionuclides are released after the container corrodes, to retard the migration of radionuclides from the corroded container to the host rock.

Bentonite, a kind of clay material, is considered the most prospective material for the buffer in a water saturated geologic medium because of its desirable properties such as low permeability, high sorption capacity, and high swelling capacity. Low permeability makes the groundwater flow slow. High sorption capacity makes the migration of radionuclides slow. However, swelling capacity, which means that bentonite can expand in volume by water uptake, has not been well understood so far. Through the excavation of tunnels before placing the waste in a geologic repository, the host rock contains fractures in addition to originally existing fractures. Given the swelling of bentonite, the fractures in the surrounding rock could be sealed by the extruded bentonite. A recent study [1] shows that if the extruded bentonite could actually seal the fractures in the host rock, the radiological toxicity of the radionuclides released from a repository could be significantly reduced. Thus, bentonite plays a key role in ensuring the safety of geologic disposal.

To investigate the expansion of bentonite through fractures, several experiments [2, 3, 4] have already been performed. Those experiments were conducted using cylindrical blocks of bentonite with water being in contact with the blocks through simulated fractures. PNC [3, 4] empirically showed that the location of the tip of expanding bentonite in a simulated planar fracture is proportional to the square root of the elapsed time after having contact with water.

In order to simulate the experimental result by PNC, a mathematical model was established by *Ahn, Chambré and Verbeke* [5] based on Terzaghi's consolidation theory [6]. With the model the movement of bentonite through fractures can be predicted as a function of time. In their model physical processes are modeled by formulating the governing equation for the space-time dependent void ratio, which is defined as the ratio of the void volume in bentonite to the solid phase volume in bentonite. The governing equation has a diffusion coefficient of water, which is composed of the viscosity and permeability of water and the compressibility of bentonite. Also, they obtained a numerical solution for the mathematical model with help of a computer code, SABRE. However, since the experiment by PNC was conducted before the mathematical model was established in their study, not all the parameter values necessary for the model calculation were measured in the experiment. For such model parameters, parametric surveys were done to determine the best choices using the available data. By doing so, they found a single set of parameters that could reproduce the experimental result.

1.2 Objective of this study

This study is motivated by the study performed by *Ahn, Chambré and Verbeke* [5] on the behavior of bentonite buffer in a geologic repository for high-level wastes, which aimed at establishing a mathematical model for the swelling of bentonite. The objective of the present study is to refine this analysis and make it more complete.

In Chapter 2, numerical simulations are conducted by running the code, SABRE, to find the best fit to the experimental result of the bentonite tip motion. As mentioned above in the previous study a single set of parameters was found to give a good agreement with the experimental curve. However, there are two parameters, the diffusion coefficient of water in the expanding bentonite and the void ratio at the tip of expanding bentonite, which can be adjusted to fit the experimental result because not all of those were measured in the experiment. Thus, a number of cases are examined to find the best fit. First, the best fit with a number of constant diffusion coefficients is examined as the simplest case. Next, a number of exponential diffusion coefficients dependent on void ratio are studied. With all these cases it is demonstrated that one can get a good agreement with the experimental result.

In Chapter 3, a new model for the tip movement of expanding bentonite is presented. The model introduced by Chambré can determine the tip position as a function of time without knowing the diffusion coefficient or the void ratio at the tip through the introduction of a single parameter that is fixed by the experiment.

In Chapter 4, the osmotic pressure concept is explored to obtain the coefficient of the compressibility in the swelling of bentonite. The model developed by *Ahn, Chambré and Verbeke* [5] has a diffusion coefficient of water, which is made up of the viscosity and permeability of water in bentonite and the compressibility of bentonite. Of these three components the compressibility was obtained by assuming the linear relationship between the void ratio and the logarithm of swelling pressure on the basis of the soil mechanics custom. However, bentonite is a special clay in view of its swelling ability. It swells to several times its dry volume when placed in contact with water [7]. Thus, it is necessary to obtain the relationship between void ratio and swelling pressure specifically applicable to bentonite. For this purpose, the osmotic pressure concept is examined. This result gives guidance to the experimentalist for the determination of the compressibility.

In Chapter 5, the conclusions of this study are summarized.

2. Numerical Simulations to Fit the Experimental Result

In this chapter we perform numerical simulations by running the code, SABRE, to find the best fit to the experimental result. In the previous study [5] a *single* set of parameters was found to give a good agreement with the experimental result. However, the mathematical model has two parameters, the diffusion coefficient of water in the expanding bentonite and the void ratio at the tip of expanding bentonite, which can be adjusted to fit the experimental result because not all of those needed for numerical simulations were measured in the experiment. Thus, we try to find more cases giving a good agreement with the experiment. We first examine the best fit with constant diffusion coefficients as the simplest case. Next, we deal with the exponential diffusion coefficient as applied in the previous report [5]. With all these results we demonstrate that several choices of diffusion coefficients can give a close agreement with the experimental result. Before going into our calculations we first summarize the results of the previous report.

2.1 Summary of the Previous Report [5]

The geometry of the experiment conducted by PNC [4] to study the expansion of bentonite through a simulated planar fracture is defined in Figure 2.1, where a water-filled horizontal fracture intersects a cylindrical block of bentonite. The bentonite is confined in a cylindrical non-deformable cell with an opening at the center, where the water-filled fracture intersects. Thus, the bentonite can come in contact with water and expand only through the horizontal planar fracture.

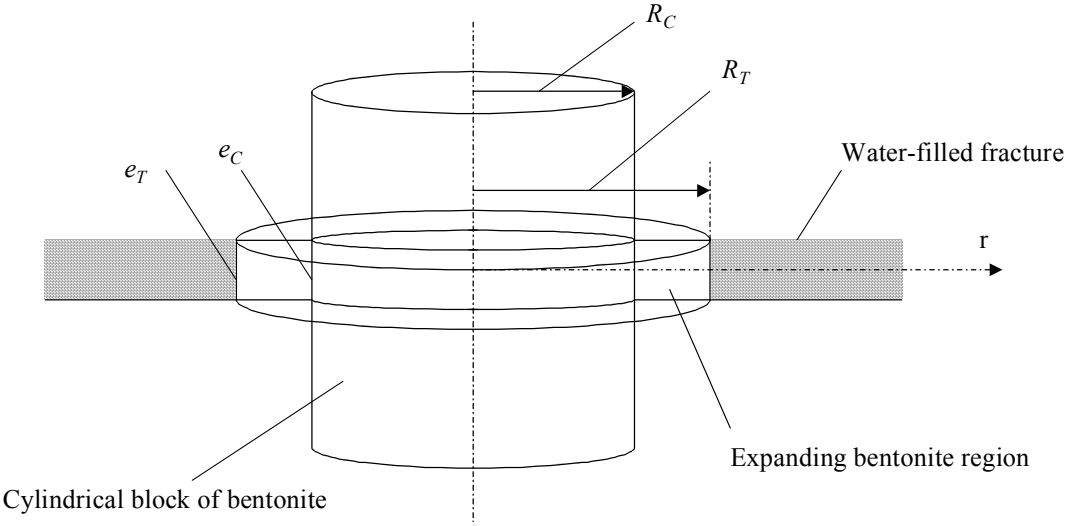

Figure 2.1 Geometrical definition of the experiment and boundary conditions.

The tip position of the expanding bentonite as a function of time used in the previous report [5] is based on an empirical relationship obtained by PNC [4] between the tip position R_T and the square root of time t,

$$R_T = 1.3\sqrt{t} + R_C,\ 0 \le t \le 100\ \text{h}, \tag{2.1}$$

as shown in Figure 2.2, where the unit accompanying 1.3 is $\text{mm} \cdot \text{h}^{-1/2}$, and the initial radius of the cylindrical block of bentonite, R_C, is 25 mm. This is based on the scattered experimental values [4].

To simulate this experimental result, a mathematical model was established by *Ahn, Chambré and Verbeke* [5] based on Terzaghi's one-dimensional consolidation theory [6]. The dimensionless quantity, void ratio e, characterizing the physical state of bentonite is used throughout the modeling. The void ratio is defined as the ratio of the void volume in bentonite to the solid phase volume in bentonite as illustrated in Figure 2.3. Clay in general has a void ratio less than unity [7]. Bentonite, however, has a void ratio far greater than unity when placed in water with all the void space in the bentonite being filled with water. Since the solid phase volume is assumed to be constant, the swelling of bentonite corresponds to the increase in void ratio in the bentonite.

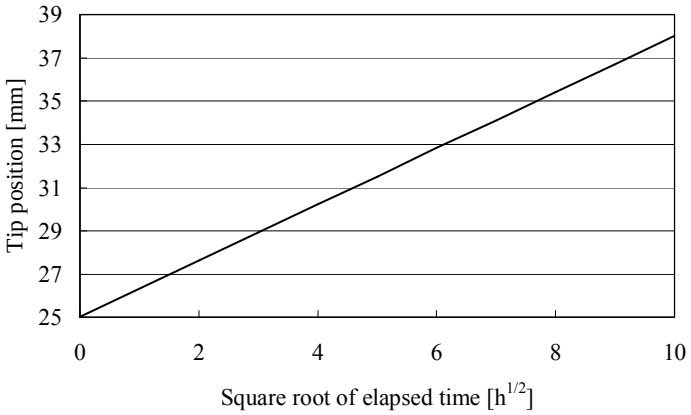

Figure 2.2 Tip position as a function of the square root of time.

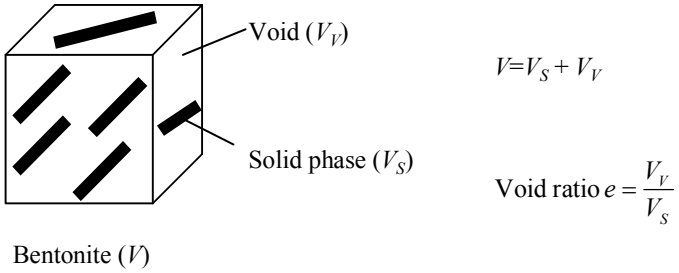

Figure 2.3 Definition of void ratio.

In the experiment, initially the void ratio is uniformly equal to e_C throughout the cylindrical block of bentonite. The expansion is considered to occur in the region $R_C \le r \le R_T$, where the bentonite is assumed to be saturated with water; namely, all the void space in the bentonite is filled with water. Water is taken up at the tip R_T and diffuses into the expanding bentonite. At $r = R_C$, water diffuses into the cylindrical block of bentonite remaining in the domain $0 \le r \le R_C$. The same volume of the bentonite with the void ratio e_C as the water volume entering the domain $0 \le r \le R_C$ extrudes into the fracture at $r = R_C$. The mathematical formulation for the space-time dependent void ratio in a one-dimensional cylindrical coordinate system is given as follows:

The mass conservation equation for water flow in water-saturated bentonite:

$$\frac{1}{1+e}\frac{\partial e}{\partial t} = \frac{1}{r}\frac{\partial}{\partial r}\left(rD(e)\frac{\partial e}{\partial r}\right), R_C \le r \le R_T, t > 0, \tag{2.2}$$

The initial and boundary conditions:

$$e(r,0) = e_C, 0 \le r \le R_T, \tag{2.3}$$

$$e(R_T,t) = e_T,\ t > 0, \tag{2.4}$$

$$e(R_C,t) = e_C,\ t > 0, \tag{2.5}$$

The governing equation for the tip position:

$$\frac{dR_T}{dt} = D(e)\frac{\partial e}{\partial r}\bigg|_{r=R_T}, t > 0, \tag{2.6}$$

The initial condition for the tip position:

$$R_T(t=0) = R_C \,. \tag{2.7}$$

where

e : void ratio [-]
$D(e)$: diffusion coefficient of water in the expanding bentonite [mm^2/h]
R_T : location of the expanding tip at time t [mm]
R_C : location of the initial tip [mm]
e_T : void ratio at the tip (constant) [-]
e_C : void ratio at the initial tip position (constant) [-].

Based on these equations, a computer code, SABRE (SAturated Bentonite Radial Expansion) was developed for the numerical solutions to the space-time dependent void ratio in the expanding bentonite [5]. The input data of SABRE consists of the diffusion coefficient, the void ratio at the tip, the initial void ratio, and the initial tip position. The output data gives the tip position as a function of time and the void ratio as a function of the radial position r.

Of these input parameters the initial void ratio e_C and the initial tip position R_C were determined by the experiment to be 0.5 and 25 mm, respectively. However, the void ratio at the tip, and the diffusion coefficient for the void ratio greater than 1.0 were not measured in the experiment. For such parameters, parametric surveys were conducted to determine the best choices. As a result of these surveys, a single case, where the void ratio at the tip is 4.05 and the void ratio dependency for the diffusion coefficient is like the one shown in Figure 2.4, was found to reproduce the experimental result.

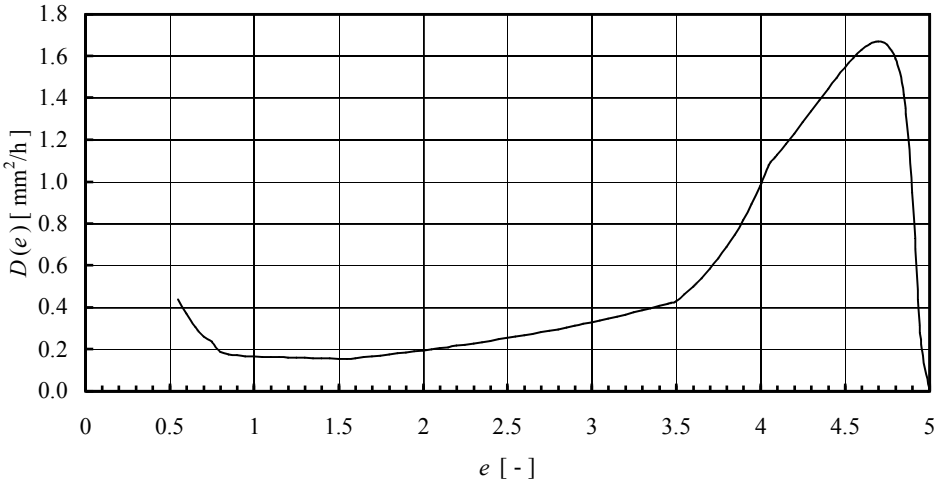

Figure 2.4 Diffusion coefficient in the report [5] to fit the experimental result.

2.2 Numerical Simulations to Fit the Experimental Curve

As described above, in the previous report [5] only one case was found to reproduce the experimental curve. The purpose of this section is to demonstrate that there are more cases giving a good agreement with the experimental curve. The mathematical model shown above has two adjustable parameters, the diffusion coefficient of water in the expanding bentonite and the void ratio at the tip of expanding bentonite. Although the diffusion coefficient is a function of void ratio in the mathematical model, we first examine the best fit with the constant diffusion coefficient as the simplest case. Next, we deal with the exponential diffusion coefficient, where the diffusion coefficient is expressed in the exponential form of void ratio as originally described in the mathematical model. These procedures have been proposed by Chambré.

2.2.1 Calculation with Constant Diffusion Coefficients

We first set the diffusion coefficient $D(e)$ equal to a constant D_0. Next, using the code SABRE we calculate

the best fit to the experimental tip position vs. square root of time curve by adjusting the void ratio at the tip e_T. Then, we change the value of the diffusion coefficient and adjust the void ratio at the tip. We repeat this procedure several times.

Seven cases for D_0 (D_0 = 0.17, 0.20, 0.30, 0.50, 1.00, 1.50, and 2.40 mm^2/h) have been calculated using the code SABRE. The values for the diffusion coefficients have been chosen referring approximately to the range of the diffusion coefficient depicted in Figure 2.4. The results are shown in Figure 2.5 a)~g). The calculated curve obtained by the code is plotted as a dashed line. The regression line obtained by applying the least squares method to the calculated curve is plotted as a solid line. Also, the equation of the regression line is shown on each figure. The regression line is defined as follows. If the conditional expected value of a random variable y, given the value of a random variable, is given by an equation $y = mx + b$, the graph of this equation is the regression line of y on x. If the regression coefficients m and b are determined by the least square methods, the regression line is expressed as $(y-\bar{y})/\sigma_y = r(x-\bar{x})\sigma_x$, where $\bar{x}, \bar{y}$ are the sample means, σ_x, σ_y are the standard deviations, and r is the sample correlation coefficient.

Figure 2.5 shows that each case gives the same regression line as the experimental curve, $R_T = 1.3\sqrt{t} + 25$, which means that there are several combinations of D_0 and e_T in agreement with the experimental result. Although case (g) seems to have the best agreement with the experimental curve, we cannot conclude anything definite about which case shows the best fit because the actual experimental values are rather scattered [4]. As far as a calculated curve gives the same regression line as the experimental curve, the calculated curve is one of the solutions that agree with the experiment.

In Table 2.1, the combinations of the diffusion coefficient and the void ratio at the tip to fit the experiment are summarized. Table 2.1 means that when the constant diffusion coefficient D_0 is prescribed, the void ratio at the tip e_T has to be adjusted in order to have an agreement with the experimental result. With this table we see that the constant diffusion coefficient D_0 decreases as the void ratio at the tip e_T increases. Equation (2.6), which expresses the speed of the tip movement, accounts for this. Equation (2.6) shows that in order to get the same expansion speed, the product of the constant diffusion coefficient and the gradient of the void ratio at the tip must be the same. The gradient of the void ratio at the tip is greater for the greater void ratio at the tip because the void ratio at the inner boundary e_C is fixed at 0.5. Consequently, the value of the constant diffusion coefficient is inversely proportional to the void ratio at the tip.

Table 2.1 Input Data to Fit the Experiment with Constant Diffusion Coefficients.

Case	D_0 [mm^2/h]	e_T [-]	e_C [-]
a	2.40	1.0	0.5
b	1.50	1.3	0.5
c	1.00	1.7	0.5
d	0.50	2.9	0.5
e	0.30	4.5	0.5
f	0.20	6.0	0.5
g	0.17	7.0	0.5

2.2.2 Calculation with Exponential Diffusion Coefficients

We set the diffusion coefficient, $D(e)$, an exponential diffusion coefficient as $D_0\exp(Ge)$, where D_0 and G are parameters. This is the form of the diffusion coefficient originally described in the mathematical model. We first let D_0 be fixed and calculate the best fit to the experimental curve by changing both G and the void ratio at the tip e_T. Then, we change D_0 and repeat the run.

Four cases for D_0 (D_0 = 0.2, 0.5, 1.0, and 2.0 mm^2/h) have been calculated using the code. In each case, four different G values (G = -0.1, 0.1, 1.0, and 2.0) have been examined as shown in Figure 2.6 a) - p). The negative value of G represents the case where the diffusion coefficient decreases as the void ratio increases. The positive value of G represents the case where the diffusion coefficient increases as the void ratio increases. The calculated curve by the code is plotted as a dashed line. The regression line obtained by applying the least squares method to the calculated curve is plotted as a solid line. Also, the equation of the regression line is shown on each figure. With these figures we find in the same way for the constant diffusion coefficient case that

each case gives the same regression line as the experimental curve, $R_T = 1.3\sqrt{t} + 25$.

In Table 2.2, the combinations of the diffusion coefficient and the void ratio at the tip to fit the experiment are summarized. Table 2.2 means that when D_0 and G are prescribed, e_T has to be adjusted in order to have an agreement with the experimental result.

Table 2.2 Input Data to Fit the Experiment with Exponential Diffusion Coefficients.

Case	D_0 [mm^2/h]	G [-]	e_T [-]	e_C [-]
a	0.2	-0.1	10.0	0.5
b	0.2	0.1	4.90	0.5
c	0.2	1.0	2.00	0.5
d	0.2	2.0	1.33	0.5
e	0.5	-0.1	3.30	0.5
f	0.5	0.1	2.50	0.5
g	0.5	1.0	1.37	0.5
h	0.5	2.0	1.00	0.5
I	1.0	-0.1	1.75	0.5
j	1.0	0.1	1.52	0.5
k	1.0	1.0	1.02	0.5
l	1.0	2.0	0.81	0.5
m	2.0	-0.1	1.12	0.5
n	2.0	0.1	1.03	0.5
o	2.0	1.0	0.80	0.5
p	2.0	2.0	0.68	0.5

2.3 Summary

The purpose of this chapter has been to demonstrate that there are several combinations of the diffusion coefficient and the void ratio at the tip giving a good agreement with the experimental curve. Two cases, the constant diffusion coefficient case and the exponential diffusion coefficient case, have been examined by running the code SABRE to get a good agreement with the experimental result. The numerical simulations show that the experimental curve determined in a time range $0 \le t \le 100$ hr can be reproduced by running the code with either constant diffusion coefficients or exponential diffusion coefficients. It has been found that the solution for the tip position vs. square root of time depends on both the diffusion coefficient and the void ratio at the tip. Therefore, the principal conclusion is that many combinations of the diffusion coefficient and the void ratio at the tip yield an agreement with the experiment. Further experiments for the diffusion coefficient and the void ratio at the tip must be conducted so that unique values can be obtained. Otherwise, according to the conclusion, the results of matching the experiment are non-unique.

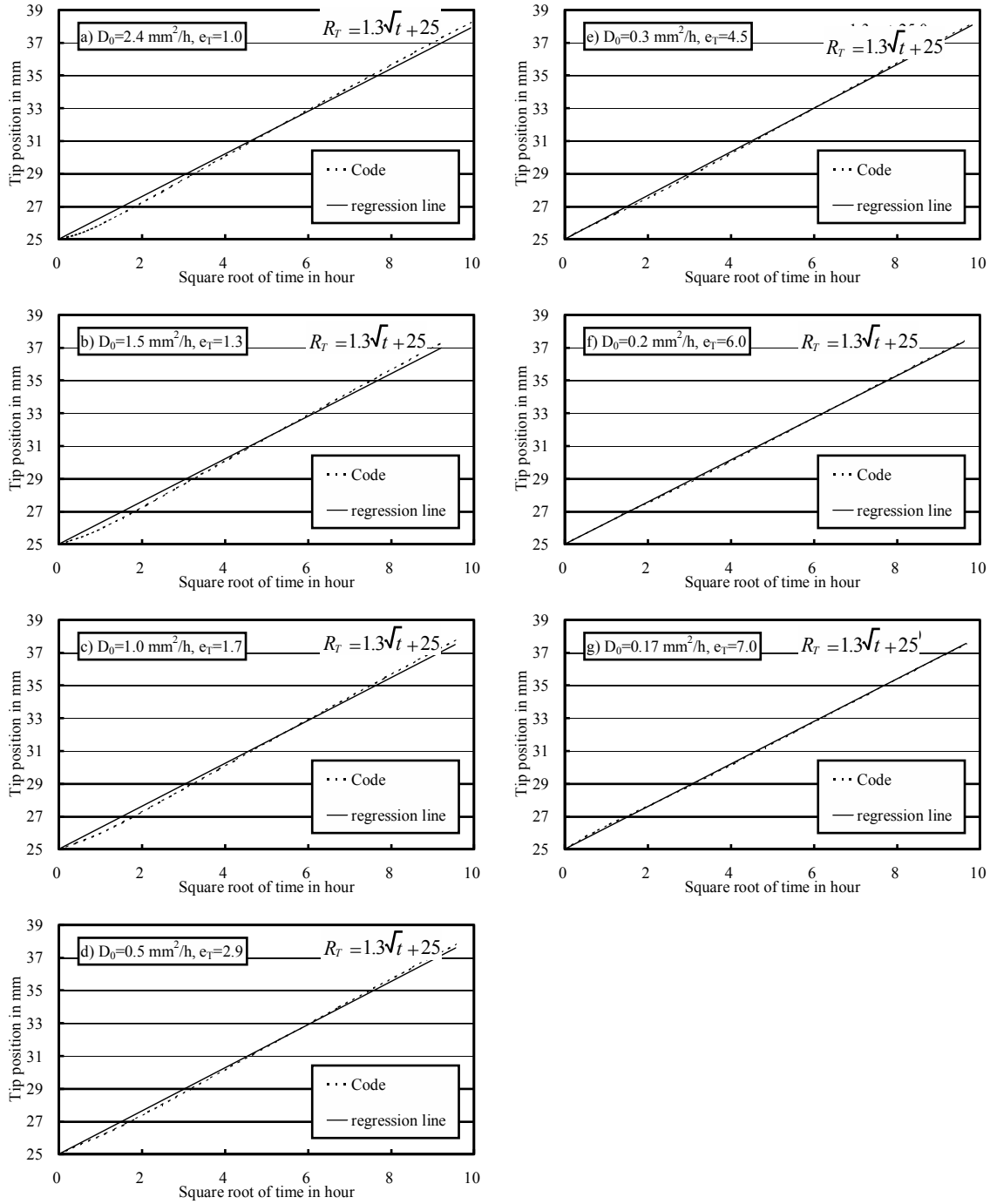

Figure 2.5 Calculated curves and their regression lines for constant diffusion coefficients to fit the experimental curve.

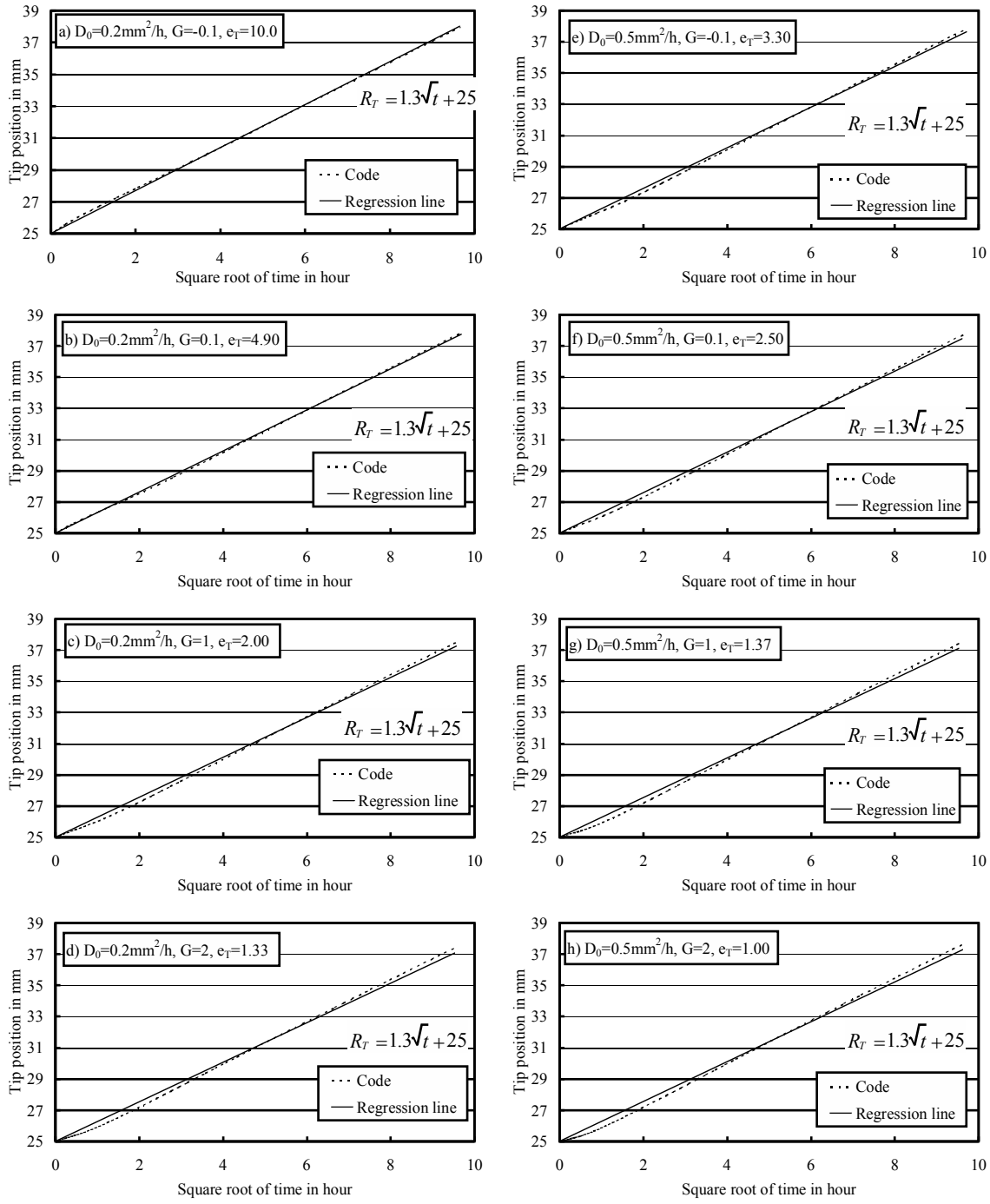

Figure 2.6 Calculated curves and their regression lines for exponential diffusion coefficients to fit the experimental curve.

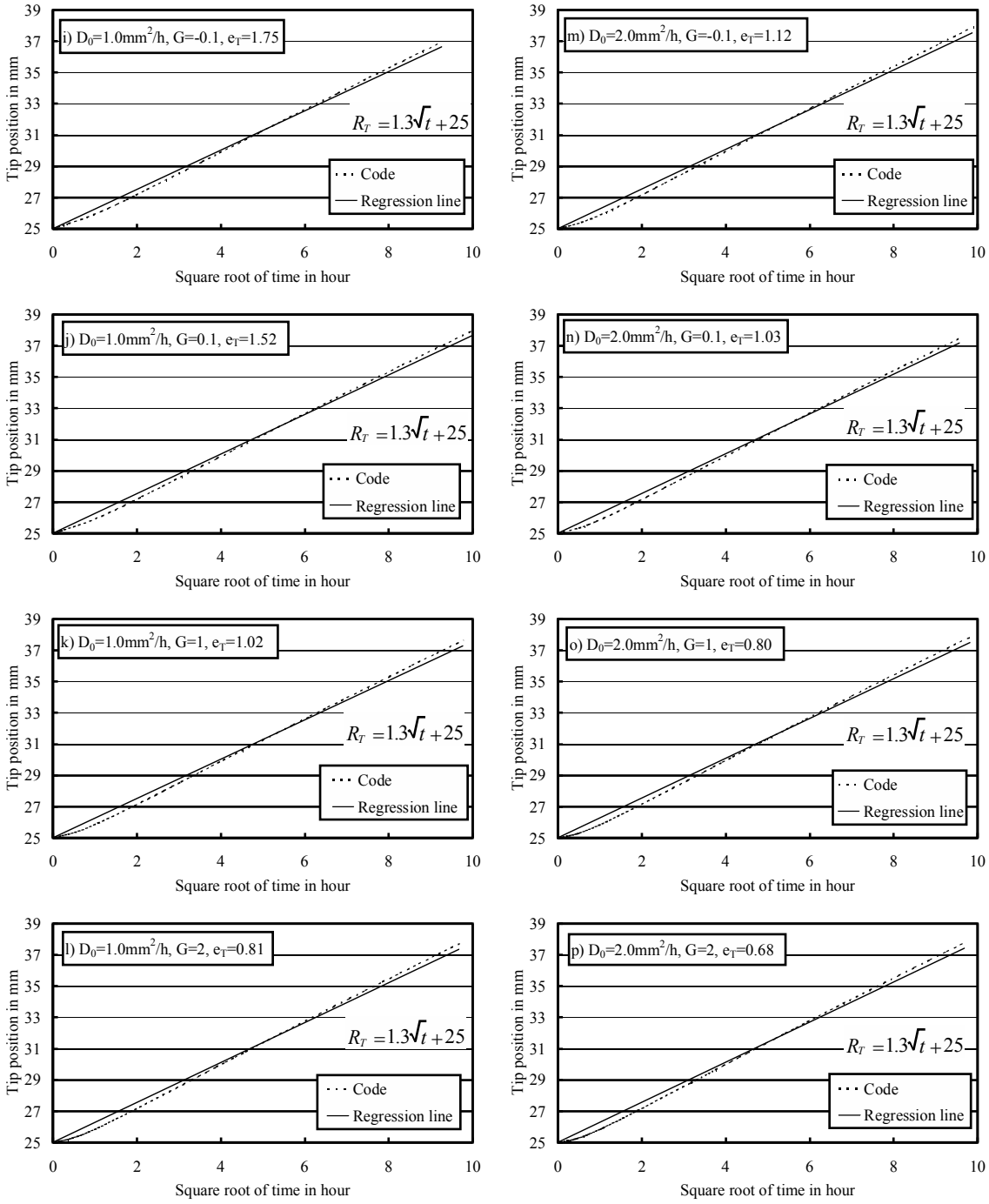

Fig.2.6. continued

3. Model 1 for the Tip Movement of Expanding Bentonite [8]

In the preceding chapter, we described our conclusion that several combinations of the diffusion coefficient and the void ratio at the tip can fit the experimental curve. Without a further experiment the present model cannot determine the diffusion coefficient and the void ratio at the tip. This chapter presents a new model for the tip movement of expanding bentonite. The model proposed by Chambré can determine the tip position as a function of time without knowing the diffusion coefficient or the void ratio at the tip through the introduction of a single parameter that is fixed by the experiment.

3.1 Model Description

As we can see from (2.6), which is the governing equation for the tip position of expanding bentonite, the calculation of the tip position requires the knowledge of the void ratio gradient de/dr at the tip position.

To evaluate de/dr, we make a principle assumption that the expansion is so slow that $e(r, t)$ is a quasi-steady state; namely, we assume that $\partial e/\partial t \cong 0$. Then, (2.2) becomes

$$0 = \frac{1}{r}\frac{d}{dr}\left(D(e) r \frac{de}{dr} \right), R_C \le r \le R_T . \tag{3.1}$$

From (3.1), using a constant, A, we can obtain on integration

$$D(e) r \frac{de}{dr} = A . \tag{3.2}$$

By separation of variables, (3.2) is written as

$$D(e) de = \frac{A}{r} dr . \tag{3.3}$$

With the side conditions in (2.4), (2.5) and (2.7), the integral of both sides of (3.3) is expressed as

$$\int_{e_C}^{e_T} D(e') de' = \int_{R_C}^{R_T} \frac{A}{r} dr , \tag{3.4}$$

where e_T : void ratio at the tip [-],
e_C : void ratio at the initial tip position [-],
R_T : location of the expanding tip [mm], and
R_C : location of the initial tip [mm].

From (3.4), the constant, A, can be written as

$$A = \frac{\beta}{\ln \dfrac{R_T}{R_C}} , \tag{3.5}$$

where

$$\beta \equiv \int_{e_C}^{e_T} D(e') de' \ \ [\mathrm{mm}^2/\mathrm{h}] \tag{3.6}$$

is the single parameter characterizing the model. Substituting (3.5) into (3.2), we obtain

$$D(e)\frac{de}{dr} = \frac{1}{r}\frac{\beta}{\ln\left(R_T / R_C \right)} . \tag{3.7}$$

At this stage we substitute (3.7) into the time-dependent (2.6), which yields

$$\frac{dR_T}{dt} = \frac{1}{R_T} \frac{\beta}{\ln\left(R_T / R_C\right)}, t > 0 . \tag{3.8}$$

Using separation of variables, (3.8) can be written as

$$R_T \ln \frac{R_T}{R_C} dR_T = \beta dt, t > 0 . \tag{3.9}$$

Dividing both sides of (3.9) by R_C^2 , (3.9) can be rewritten as

$$\frac{R_T}{R_C} \ln \frac{R_T}{R_C} \frac{dR_T}{R_C} = \frac{\beta}{R_C^2} dt, t > 0 . \tag{3.10}$$

Now set $\frac{R_T}{R_C} \equiv x$, then (3.10) becomes

$$x \ln x dx = \frac{\beta}{R_C^2} dt, t > 0 . \tag{3.11}$$

With the initial condition given by (2.7), the integral of both sides is expressed as

$$\int_1^x x \ln x dx = \int_0^t \frac{\beta}{R_C^2} dt. \tag{3.12}$$

Applying partial integration to the left hand side gives the implicit solution for the dimensionless tip position $\tau = \tau(x)$ as

$$\left\{\left(\frac{x^2}{2} \ln x - \frac{x^2}{4}\right) + \frac{1}{4}\right\} = \tau, x \geq 1, \tau \geq 0 , \tag{3.13}$$

where

$$\tau \equiv \frac{\beta}{R_C^2} t \ [\text{-}], \ t \geq 0 . \tag{3.14}$$

Equation (3.13) shows that the relationship between x and τ is not determined by the *D(e)* function and e_T but by β.

Since our objective of this analysis is to determine x as a function of time, we turn now to the explicit solution of (3.13).

3.2 Graphical Solution

One method to do this is a graphical solution. A graph of $\tau(x)$ is plotted in Figure 3.1. The line $\tau = x$ is also shown on the figure. The inverse function, $x(\tau)$, which is the solution for the tip position, is obtained graphically by reflecting the graph of $\tau(x)$ in a mirror held along the line $\tau = x$ [9]. Also, the name of each axis must be exchanged when using this reflection. The obtained explicit solution to (3.13), $x = x(\tau)$ is given in Figure 3.2.

Furthermore, to compare with the experimental curve we plot x vs. $\sqrt{\tau}$ in Figure 3.3, which shows a linear trend. Strictly speaking, this curve is not exactly linear because the derivative of x decreases gradually as shown in Figure 3.4. However, the experiment was not accurate enough to say that the relationship between the tip position and the square root of time is precisely linear. Chambré has shown that the change in $dx/d\sqrt{\tau}$ with $\sqrt{\tau}$ is a property of the radial expansion of the bentonite in the cylindrical fracture.

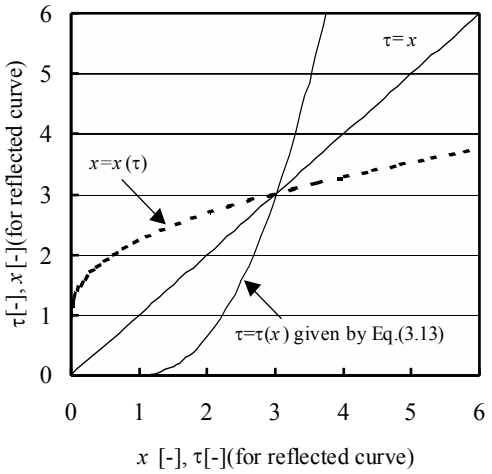

Figure 3.1 Inversion by reflection in τ=*x*.

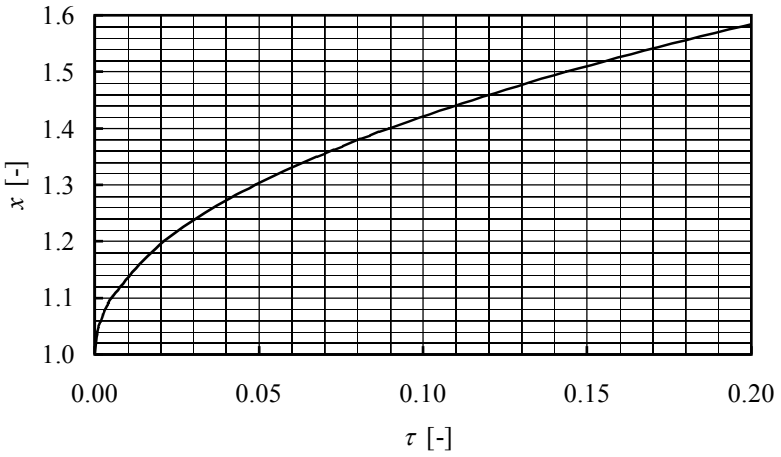

Figure 3.2 *x* as a function of τ obtained by the graphical solution.

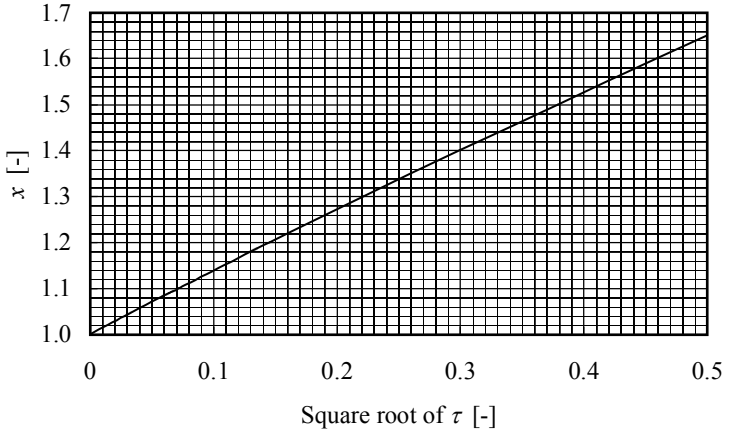

Figure 3.3 *x* as a function of square root of τ obtained by the graphical solution.

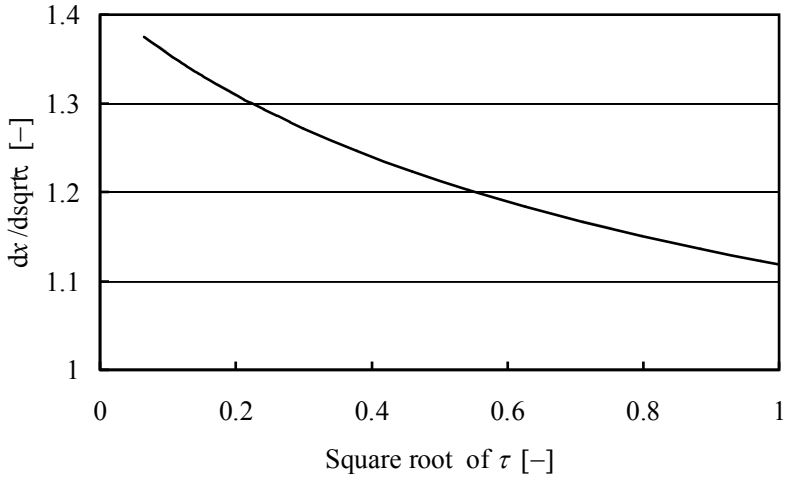

Figure 3.4 Derivative of $x(\sqrt{\tau})$.

3.3 Analytical Solution

3.3.1 Derivation

The other way to obtain the explicit solution of (3.13) for $x(\tau)$ is to solve this equation by analytical means.

Equation (3.13) can be rewritten as

$$x^2 \ln x^2 - x^2 = 4\tau - 1, x \geq 1, \tau \geq 0 . \tag{3.15}$$

Since $x \geq 1$, set

$$x(\tau) = \exp(\phi(\tau)),\ \phi(\tau) \geq 0 . \tag{3.16}$$

Once $\phi(\tau)$ is known, we have the explicit solution.

Substituting (3.16) into (3.15) gives

$$(2\phi(\tau) - 1)\exp(2\phi(\tau)) = 4\tau - 1,\ \tau \geq 0 . \tag{3.17}$$

Dividing both sides of (3.17) by e yields

$$(2\phi(\tau) - 1)\exp(2\phi(\tau) - 1) = \frac{4\tau - 1}{\mathrm{e}},\ \tau \geq 0 . \tag{3.18}$$

By setting

$$z = \frac{4\tau - 1}{\mathrm{e}}, \tau \geq 0 , \tag{3.19}$$

and

$$w(z) = 2\phi(\tau) - 1 , \tag{3.20}$$

in (3.18), there results

$$w(z) \cdot \exp\{w(z)\} = z . \tag{3.21}$$

Euler studied this equation and presented a power series development of (3.21) in the form,

$$w(z)=\sum_{n=1}^{\infty}\frac{(-n)^{n-1}}{n!}z^n,\ -\frac{1}{\mathrm{e}}<z<\infty. \tag{3.22}$$

A formal derivation of (3.22) is obtained in the next section.

At any rate, with $w(z)$ known one can solve (3.20) for

$$\phi(\tau)=\frac{1}{2}\Big(w(z)+1\Big), \tag{3.23}$$

and with (3.19),

$$\phi(\tau)=\frac{1}{2}\left\{w\left(\frac{4\tau-1}{\mathrm{e}}\right)+1\right\}. \tag{3.24}$$

Therefore, substituting (3.24) into (3.16) gives the explicit expression for the inverse function $x(\tau)$ of (3.13),

$$x(\tau)=\exp\left\{\frac{1}{2}w\left(\frac{4\tau-1}{\mathrm{e}}\right)+\frac{1}{2}\right\},\ \tau\ge 0, \tag{3.25}$$

where the function w is given by the power series in (3.22).

Furthermore it follows from (3.21) that when $\tau=0$,

$$w\left(-\frac{1}{\mathrm{e}}\right)=-1. \tag{3.26}$$

So (3.25) shows that the initial condition in equation (2.7), $x(0)=1$, is satisfied.

3.3.2 Verification of the Solution and Some Numerical Results

Equation (3.8), which is the governing equation for the tip position, can be rewritten in terms of x and τ as

$$\frac{dx}{d\tau}=\frac{1}{x\ln x},\ \tau>0. \tag{3.27}$$

We formally verify that (3.25) satisfies (3.27). First, we find the derivative of (3.25).

By (3.16),

$$x(\phi)=\exp(\phi(\tau)). \tag{3.28}$$

Then,

$$\frac{dx}{d\tau}=\frac{dx}{d\phi}\cdot\frac{d\phi}{d\tau}=\exp(\phi)\frac{d\phi}{d\tau}, \tag{3.29}$$

and with (3.24),

$$\frac{d\phi}{d\tau}=\frac{1}{2}\frac{d}{d\tau}w\left(\frac{4\tau\text{-}1}{\mathrm{e}}\right). \tag{3.30}$$

Let $z(\tau)\equiv\dfrac{4\tau\text{-}1}{\mathrm{e}}$, then for $w(z(\tau))$

$$\frac{d}{d\tau}\Big[w(z(\tau))\Big]=\frac{d}{dz}\Big[w(z(\tau))\Big]\cdot\frac{dz}{d\tau}=4\mathrm{e}^{-1}\frac{dw(z)}{dz}. \tag{3.31}$$

Thus, we obtain from (3.29) – (3.31)

$$\frac{dx}{d\tau} = \exp(\phi) \cdot 2\mathrm{e}^{-1} \cdot \frac{dw(z)}{dz}. \tag{3.32}$$

From the defining equation of $w(z)$ in (3.21), we obtain by differentiation

$$\frac{dw(z)}{dz} = \frac{1}{\exp(w(z))(1+w(z))}. \tag{3.33}$$

Substituting this into (3.32) gives

$$\frac{dx}{d\tau} = \frac{2}{1+w(z)} \exp(\phi - 1 - w(z)). \tag{3.34}$$

But by (3.28)

$$x = \exp(\phi) \text{ or } \phi = \ln x \tag{3.35}$$

and with (3.20)

$$\frac{1+w}{2} = \phi = \ln x. \tag{3.36}$$

Hence (3.34) reduces to

$$\frac{dx}{d\tau} = \frac{1}{x \ln x}. \tag{3.37}$$

Therefore, (3.25) has been found to satisfy (3.27).

The computation of the derivative dw/dz in (3.33) can be extended to higher derivatives by utilizing the principal generating function (3.21). If the first four derivatives about z=0 are calculated, the following results are obtained:

$$\begin{aligned} w^{(1)}(0) &= 1, \\ w^{(2)}(0) &= -2, \\ w^{(3)}(0) &= 9, \\ w^{(4)}(0) &= -64, \end{aligned} \tag{3.38}$$

which suggests the following generalization:

$$w^{(n)}(0) = (-n)^{n-1}. \tag{3.39}$$

This leads formally to the following MacLaurin expansion:

$$w(z) = \sum_{n=1}^{\infty} \frac{(-n)^{n-1}}{n!} z^n, \tag{3.40}$$

which agrees with the power series in equation (3.22).

For this expansion the asymptotic expansion about $z = -\mathrm{e}^{-1}$,

$$w(z) \approx -\frac{5}{3} + \sqrt{2z\mathrm{e}+2} - \frac{2}{3} z\mathrm{e} + \frac{11}{72}(2z\mathrm{e}+2)^{3/2} - \frac{43}{540}(2z\mathrm{e}+2)^{2} + \frac{559}{17280}(2z\mathrm{e}+2)^{5/2}, \tag{3.41}$$

is available for $-\mathrm{e}^{-1} \le z < -0.28$.

The following numerical table has been prepared from these expansions.

The function $w(z)$ calculated with the help of Table 3.1 are plotted in Figure 3.5. With Figure 3.5, the explicit solution for $x(\tau)$ in (3.25) is plotted in Figure 3.6 with respect to τ and in Figure 3.7 with respect to $\sqrt{\tau}$, both of which are the same as Figure 3.2 and Figure 3.3, respectively.

Table 3.1 Function $w(z)$

z	$w(z)$	z	$w(z)$	z	$w(z)$
-0.36	-0.806	-0.23	-0.315	-0.10	-0.112
-0.35	-0.717	-0.22	-0.296	-0.09	-0.0994
-0.34	-0.654	-0.21	-0.277	-0.08	-0.0873
-0.33	-0.603	-0.20	-0.259	-0.07	-0.0755
-0.32	-0.560	-0.19	-0.242	-0.06	-0.0640
-0.31	-0.523	-0.18	-0.226	-0.05	-0.0527
-0.30	-0.489	-0.17	-0.210	-0.04	-0.0417
-0.29	-0.459	-0.16	-0.194	-0.03	-0.0309
-0.28	-0.431	-0.15	-0.179	-0.02	-0.0204
-0.27	-0.405	-0.14	-0.165	-0.01	-0.0101
-0.26	-0.380	-0.13	-0.151	0	0
-0.25	-0.357	-0.12	-0.138		
-0.24	-0.336	-0.11	-0.125		

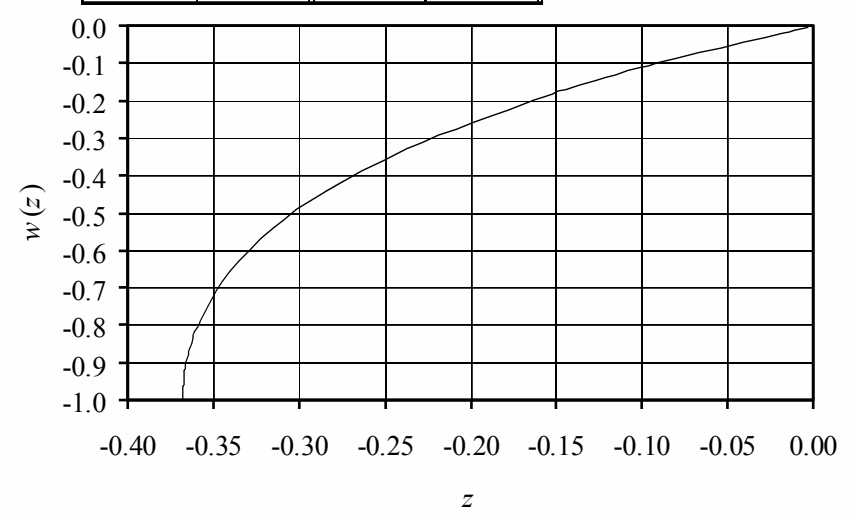

Figure 3.5 Function $w(z)$.

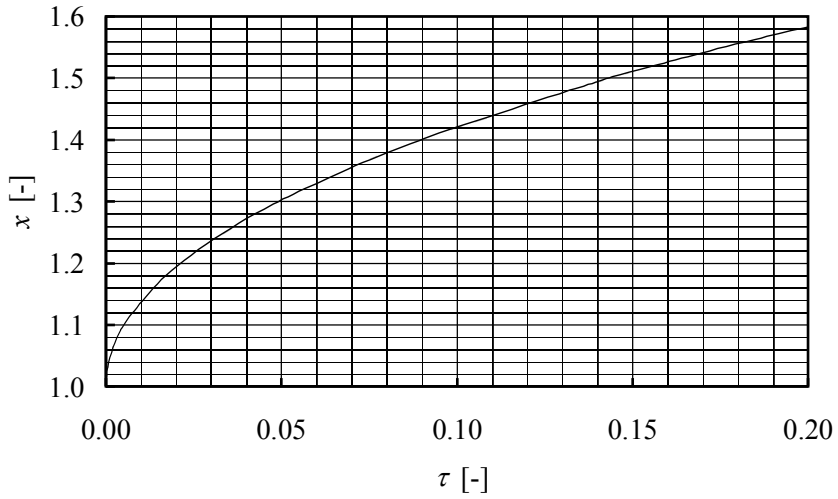

Figure 3.6 x as a function of τ obtained by the analytical solution.

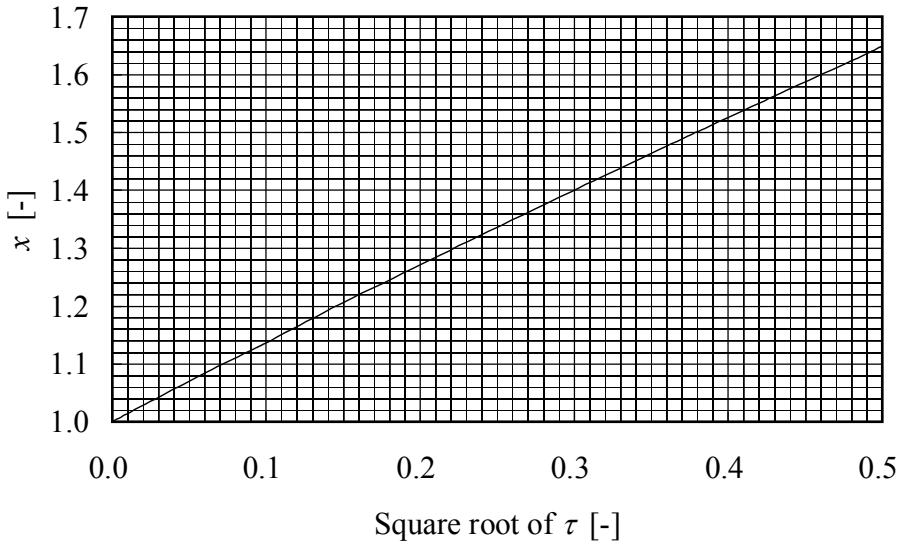

Figure 3.7 ***x*** **as a function of square root of τ obtained by the analytical solution.**

3.4 How to Use Model 1

Here we describe how Model 1 can be used to fit the experimental curve. As mentioned above Model 1 has a single adjustable parameter β that must be fixed through the fitting to the experimental curve. We first prepare the experimental curve in terms of x and $\sqrt{t}$. Dividing the both sides of (2.1) by R_C^2 yields

$$x = \frac{1.3}{R_C}\sqrt{t} + 1, \; t \geq 0, \tag{3.42}$$

where the initial radius of the cylindrical block of bentonite, R_C, is 25 mm. Equation (3.42) is plotted in Figure 3.8.

Then, the fitting is done using either the graphical solution or the analytical solution.

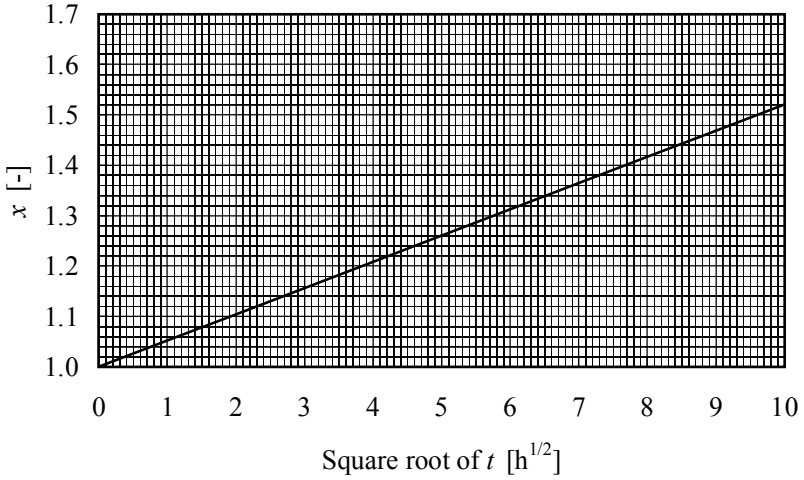

Figure 3.8 ***x*** **as a function of square root of *t* obtained by the experiment.**

3.4.1.1 With Graphical Solution

Taking the square root of both sides of (3.14), we obtain the following relationship between $\sqrt{\tau}$ and $\sqrt{t}$:

$$\sqrt{\tau} = \sqrt{\frac{\beta}{R_C^2}}\sqrt{t}, t \geq 0 . \tag{3.43}$$

With (3.43) and some β value, Figure 3.3 can be converted to the graph of x versus $\sqrt{t}$. Comparing this converted graph with the experimental curve in Figure 3.8, β is determined to get the best fit.

3.4.1.2 With Analytical Solution

Combining (3.25) and (3.43) gives x as a function of $\sqrt{t}$ with β as an adjustable parameter,

$$x = \exp\left\{\frac{1}{2}w\left(\frac{4\cdot\frac{\beta}{R_C^2}\left(\sqrt{t}\right)^2 - 1}{\mathrm{e}}\right) + \frac{1}{2}\right\},\ t \geq 0 , \tag{3.44}$$

where the function w is given by Table 3.1.

Fitting the curve obtained by (3.44) to the experimental curve requires two points. One is obviously the initial tip position at $t = 0$ [h]. The other is an arbitrary point between $t = 0$ [h] and $t = 100$ [h]. Suppose this point is set at t^* [h]. The value of w can be calculated by equating (3.42) and (3.44) as

$$\frac{1.3}{R_C}\sqrt{t^*} + 1 = \exp\left\{\frac{1}{2}w\left(\frac{4\cdot\frac{\beta}{R_C^2}\left(\sqrt{t^*}\right)^2 - 1}{\mathrm{e}}\right) + \frac{1}{2}\right\}. \tag{3.45}$$

Then, the argument of w is determined with the help of Table 3.1, which finally gives β.

With both methods, it has been found that Model 1 shows a good agreement with the experimental curve in a time range $0 \leq t \leq 100$ hr when β is fixed at 0.95 as shown in Figure 3.9.

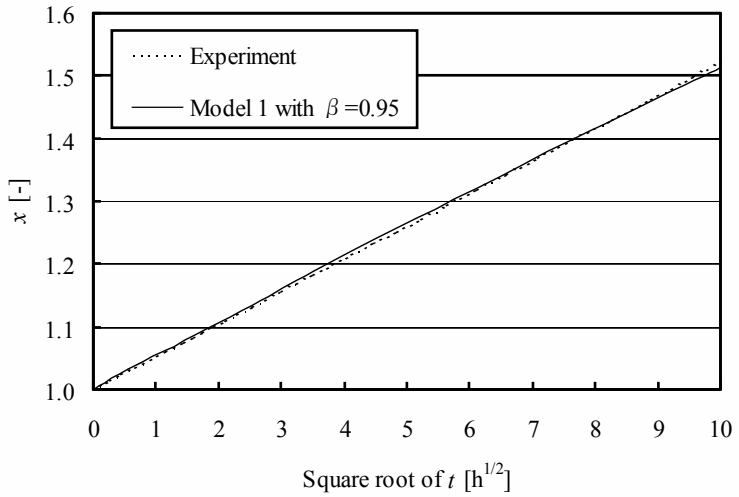

Figure 3.9 Comparison of the experimental curve and the curve obtained by Model 1 with β=0.95.

3.5 Summary

A new model, Model 1, to calculate the tip position of expanding bentonite as a function of time has been introduced by Chambré. Model 1 enables us to determine the tip position as a function of time without knowing the diffusion coefficient or the void ratio at the tip through the introduction of a single parameterβ. β is determined through the fitting of the curve obtained by Model 1 to the experimental curve. As a result of the fitting in a time range $0 \le t \le 100$ hr, β is fixed at 0.95.

As pointed out in Chapter 2, at this stage the previous model [5] cannot determine the two key parameters of the model, the diffusion coefficient and the void ratio at the tip, without a further experiment. The significance of Model 1 comes from its capability of determining the tip position without the information of the diffusion coefficient or the void ratio at the tip. Further, Model 1 does not require a large computer code. Two solutions, the graphical solution and the analytical solution, are available.

4. Application of Osmotic Pressure Concept to Swelling of Bentonite [8]

In this chapter we explore the osmotic pressure concept to obtain the coefficient of the compressibility in the swelling of bentonite. The model developed by *Ahn, Chambré and Verbeke* [5] has a diffusion coefficient of water, which is made up of the viscosity and permeability of water and the compressibility of bentonite. Of these three components they obtained the compressibility by assuming the linear relationship between the void ratio and the logarithm of swelling pressure on the basis of the soil mechanics custom [7]. However, bentonite is a special clay in view of its swelling ability. It swells to several times its dry volume when placed in contact with water. Thus, we need the relationship between void ratio and swelling pressure specifically applicable to bentonite. For this purpose we examine the osmotic pressure concept. First, the concept of osmotic pressure in general is described. Then, why the osmotic pressure concept can be applied to the swelling of bentonite is explained and the relationship between void ratio and swelling pressure is presented. Finally, the coefficient of compressibility is discussed.

4.1 Osmotic pressure

The osmotic pressure phenomenon involves a semipermeable membrane, some film that has pores large enough to allow passage of small solvent molecules but small enough to prevent passage of large solute molecules of high molecular weight [10]. If a solution is separated from its pure solvent by a semipermeable membrane, some of the pure solvent passes through the membrane into the solution, as shown in Figure 4.1. This process of penetration of the pure solvent through the semipermeable membrane is called osmosis. The flow stops and the system reaches equilibrium after the solution side has risen to a height determined by the concentration of the solution. Under these equilibrium conditions, the solution is under a greater hydrostatic pressure than the pure solvent. The difference of the height between the solution side and the solvent side h, multiplied by the density of the solution side $\rho_{solution}$ and the acceleration due to the gravity g, gives the extra pressure on the solution, and this is the osmotic pressure,

$$P = \rho_{\text{solution}} \cdot g \cdot h \,. \tag{4.1}$$

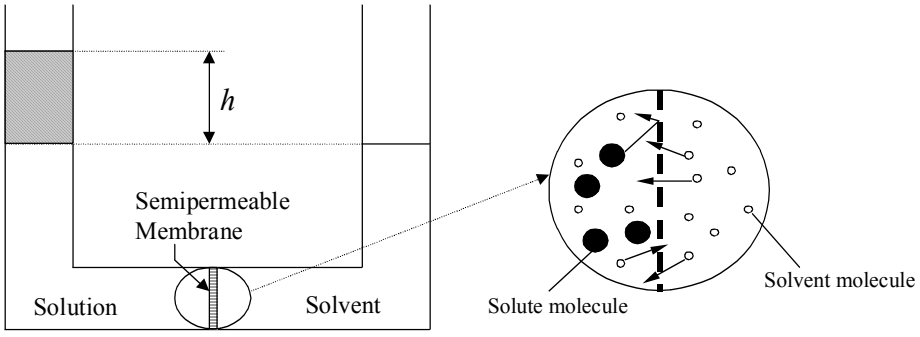

Figure 4.1 Osmotic pressure phenomenon.

From experimental measurements on dilute solutions of known concentrations, van't Hoff has found by analogy with the ideal gas law that the relationship between osmotic pressure and concentration is simply

$$P = cRT \,, \tag{4.2}$$

where c is the molar concentration of solute, R is the gas constant, and T is the absolute temperature. Equation (4.2) can also be derived rigorously by using the methods of thermodynamics [11]. If (4.2) holds for several species, (4.2) can be generalized as

$$P = RT\sum_i (c_A^{(i)} - c_B^{(i)}) \,, \tag{4.3}$$

where A and B stand for the solutions with different concentrations in the two compartments separated by the membrane as illustrated in Figure 4.2, and i stands for the kind of species.

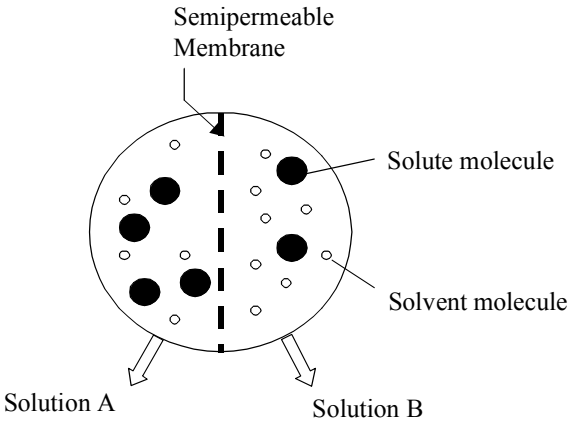

Figure 4.2 Two solutions separated by the semipermeable membrane.

4.2 Application of the Osmotic Pressure Concept to the Swelling of Bentonite

In clay, there is no true semipermeable membrane separating regions of high and low ion concentration. The effect of a restrictive membrane is introduced, however, by the influence of the negatively charged clay surfaces on the attracted cations. Because of the attraction of cations to clay particle surfaces, the cations are not free to diffuse; thus, concentration differences responsible for osmotic pressures are developed. The difference in osmotic pressure midway between particles and in the equilibrium solution surrounding the clay causes the interparticle repulsive pressure or swelling pressure. To apply this theory to bentonite, we assume two things: 1) the surfaces of bentonite particles are negatively charged, and 2) bentonite particles are plate-shaped or tabular. Thus, we first address clay structure; then, we describe the model to calculate the swelling pressure. Finally we present a numerical example of void ratio versus swelling pressure calculated by this model.

4.2.1 Clay Structure

Particles with a diameter smaller than 1 μ m but larger than molecular size (1 nm) are classified as colloids, or are said to be in the colloid state [12]. Clay particles fall within this range. Their small size gives them a large surface area relative to volume, which means that the surface properties of colloids may dominate their behavior. The surface properties of larger particles are usually neglected due to the dominance of gravity and hydrodynamic forces. Species smaller than colloids are generally considered on a purely molecular level.

The main clay mineral in bentonite is montmorillonite (also identified as smectite), which is made up of an alumina sheet sandwiched between two silica sheets [13] as shown in Figure 4.3. The silicon unit consists of a silicon atom surrounded by four oxygen atoms in tetrahedron coordination. Combining the silicon units gives the silica sheet. The alumina unit consists of an aluminum atom equidistant from six hydroxyls in octahedral coordination. Combining the alumina units gives the alumina sheet. In montmorillonite, there is isomorphous (meaning "same form") substitution of one magnesium atom with +2 valence for every six aluminum atoms with +3 valence in the alumina sheet, which causes a net unit charge deficiency. This is the reason for the negative charge of clay surfaces. Isomorphous substitution could occur if a magnesium atom were more readily available at the site than an aluminum atom during the formation of the mineral. The theoretical composition without isomorphous substitutions is $(OH)_4Si_8Al_4O_{20} \cdot n(\text{interlayer})H_2O$. Due to the isomorphous substitutions the composition formula for montmorillonite is $(OH)_4Si_8(Al_{3.34}Mg_{0.66})O_{20} \cdot n(\text{interlayer})H_2O$ [13].

The montmorillonite particle carries sodium or calcium ions to compensate the charge deficiency on the particle. These sodium or calcium ions are termed exchangeable cations because one cation can be easily replaced by another with equal valence, or by two with one-half valence of the original one when the montmorillonite particle is placed in water. The exchangeable cations are not all held in a layer right at the clay surface, but are present at some average distance from the surface. The lower the valence, the greater is the average distance from the surface. The electrical force between negatively charged surface and positively charged ions attracts the cations to the surface, but their thermal energy makes them diffuse away from this

space with a high ion concentration. The balance of Coulomb electrical attraction and thermal diffusion leads to a diffuse layer of cations, with the concentration highest at the surface and gradually decreasing with distance from the surface. These charged surface and distributed charge in the adjacent phase are together termed the diffuse double layer [13], which can be visualized as illustrated in Figure 4.4. The Debye length is a measure of the "thickness" of the diffuse double layer. The theory of the diffuse double layer was worked out by Gouy and Chapman, and modified by Stern [12]. The main assumptions in the derivation of the theoretical distribution of ions in the diffuse layer are that the clay particle is considered a simple charged plate for which the electric field is described by the Poisson's equation, and that the distribution of ions in this field is described by the Boltzmann distribution function. The interaction of the diffuse double layer gives an explanation for the properties of swelling.

The montmorillonite may occur, in ultimate dispersion, as a particle plate (10 Å) thick. Variation in the other two dimensions of clay particles is related to the degree of crystallinity of the clay minerals. A typical particle of montmorillonite has the dimensions of 1000 Å×1000 Å×10 Å [14], which produces a specific surface area of about 800 m^2/g of clay. If all particles contained in about 10 g of this clay could be spread out side by side, they would cover an area of about 90 m×90 m. Surface area could be calculated if the size and shape distributions of the soil particles were known, but this method is impractical. Surface area is therefore determined experimentally by measuring the amount of a liquid or gas required to cover the surface. Water vapor, nitrogen and organic liquids such as ethylene glycol are used. A method based on the weight of ethylene glycol adsorbed as a monomolecular layer on the clay surface is widely used [7].

Clays containing the montmorillonite mineral expand in volume when placed in contact with water. When water becomes available the combinations of silica-alumina-silica sheets that comprise the montmorillonite mineral remains intact, but the minerals are layered similar to pages assembled in a book to form a clay particle as described above, and it is between these layers where the volume of water increases or decreases. The volume change is related to the thickness of water adsorbed between the layers of montmorillonite minerals.

In summary it is reasonable to assume that the montmorillonite is a plate-shaped expansive clay mineral with its surface negatively charged.

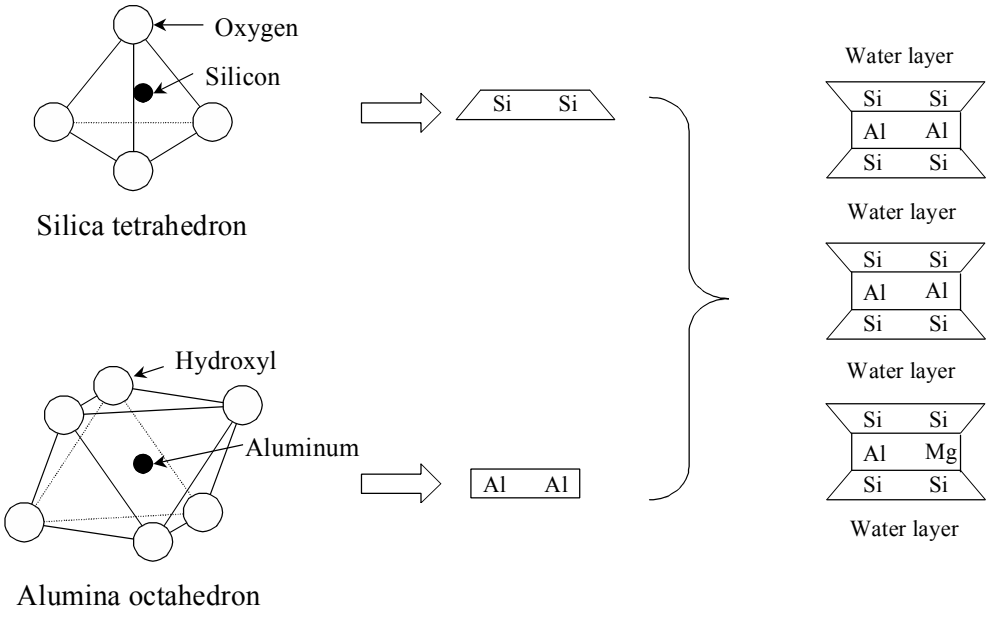

Figure 4.3 Schematic representation of typical montmorillonite structure.

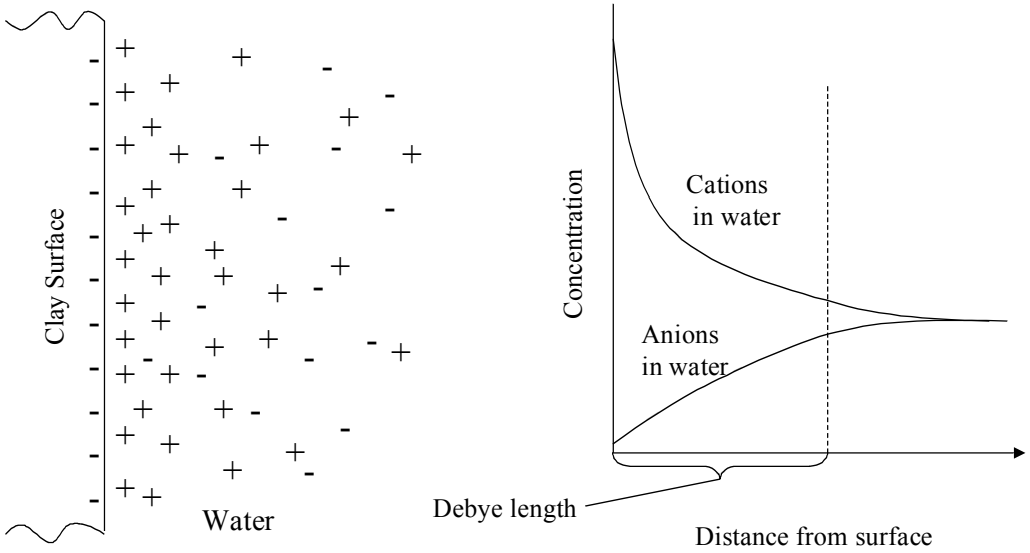

Figure 4.4 Distribution of ions adjacent to a clay surface according to the concept of the diffuse double layer.

4.2.2 Model to Calculate the Swelling Pressure

We consider a water saturated assembly of montmorillonite particles. The ion distribution for interacting montmorillonite particles rather than the ion distribution around a single particle is of interest in interpreting montmorillonite behavior. From this viewpoint let us focus on two parallel flat plates in the assembly separated at distance 2*d*, where the diffuse double layer of each plate overlaps as illustrated in Figure 4.5. The situation in Figure 4.5 with a fictitious membrane is similar to that illustrated in Figure 4.2. We assume that the montmorillonite contains a single electrolyte such as sodium chloride. Then, from (4.3) the swelling pressure, P_s, is calculated as the osmotic pressure due to the difference in concentration of ions between clay plates and in the bulk water:

$$P_s = RT\left[(c_c + c_a) - (c_c^0 + c_a^0)\right], \tag{4.4}$$

where c_c and c_a are the midplane concentrations of cations and anions between the plates, and c_c^0 and c_a^0 are the equilibrium concentrations of cations and anions in the bulk water outside the plates. The osmotic pressure, of course, gives only the repulsive forces. Since we do not consider the attractive van der Waals' forces also in operation, the swelling pressure calculated by this approach could therefore be high but the error is known to be small at least at larger interparticle distances such as the ones corresponding to void ratios greater than about 1.8 [15].

At equilibrium in dilute solutions, Guoy made the concentration equilibrium assumption,

$$c_c \cdot c_a = c_c^0 \cdot c_a^0 . \tag{4.5}$$

On the other hand, from charge neutrality in the bulk water we have

$$c_c^0 = c_a^0 \equiv c^0 . \tag{4.6}$$

Combining (4.5) and (4.6) gives

$$c_a = \frac{(c^0)^2}{c_c} . \tag{4.7}$$

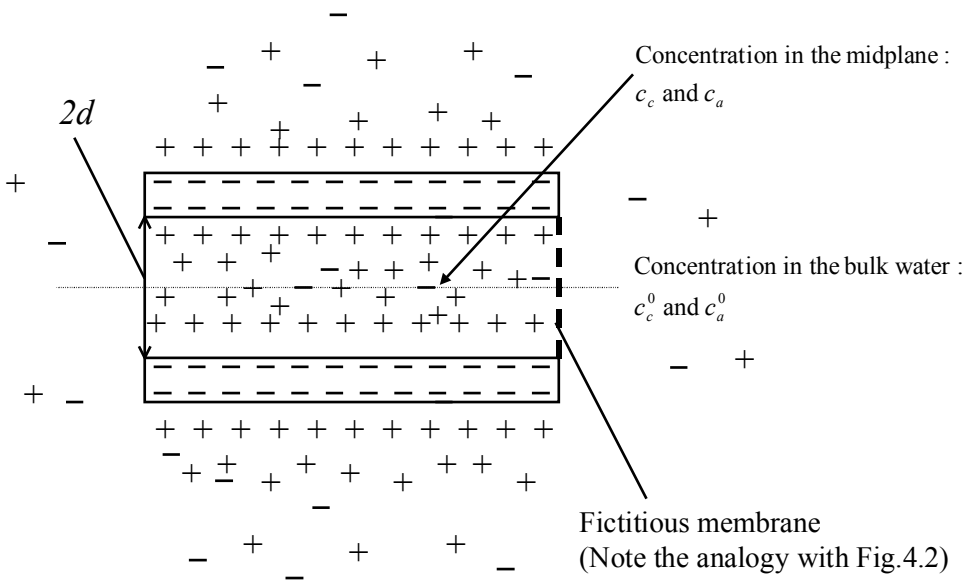

Figure 4.5 Model to calculate the osmotic pressure generated between two plates.

Here Chambré introduced the ion ratio, *r*, as the primary variable,

$$\frac{c^0}{c_c} \equiv r\,, \tag{4.8}$$

where $0 < r < 1$ because $0 < c^0 < c_c$. Then (4.4) becomes

$$P_s = RTc^0\left(\frac{1}{r} + r - 2\right),\ 0 < r < 1\,. \tag{4.9}$$

From the solution of the double layer distribution between two plates Chambré verified the relationship between the half spacing *d* and the ion ratio *r* as

$$\frac{d}{D_b} = 2\sqrt{r}\left\{K\left(r, \frac{\pi}{2}\right) - F\left(r, \arcsin\left(\exp\left(-\frac{z}{2}\right)\cdot r\right)\right)\right\},\ 0 < r < 1\,, \tag{4.10}$$

where $K(r, \pi/2)$ is the complete elliptic integral of the first kind, $F(r, \alpha)$ is the elliptic integral of the first kind, D_b is the Debye length, and *z* is the dimensionless plate surface potential. Values for the elliptic integrals are given in a standard table [16]. The Debye length is a measure of the "thickness" of the double layer and expressed as

$$D_b = \sqrt{\frac{\varepsilon kT}{2n^0 e^2 \nu^2}}\,, \tag{4.11}$$

where ε is the dielectric constant of water, *k* is the Boltzmann constant, *T* is the absolute temperature, n^0 is the number of ions per unit volume in the bulk water away from the influence of the surface, *e* is the electronic charge, and ν is the ionic valence. This relationship shows that the Debye length varies inversely with the valence and the square root of the concentration and directly with the square root of the dielectric constant and temperature, other factors remaining constant.

When *z*, the dimensionless plate surface potential, is large enough, which is the case for montmorillonite, $\exp\left(-z/2\right)r$ becomes zero, which in turn makes the elliptic integral $F(r,0)$ zero. Thus, we consider a reduced form of (4.10),

$$\frac{d}{D_b} = 2\sqrt{r}K\left(r, \frac{\pi}{2}\right),\ 0 < r < 1, \tag{4.12}$$

where

$$K\left(r, \frac{\pi}{2}\right) = \int_0^{\pi/2} \left(1 - r^2 \sin^2\theta\right)^{-1/2} \mathrm{d}\theta,\ 0 < r < 1. \tag{4.13}$$

The graph of K versus r is plotted in Figure 4.6 with the help of [16].

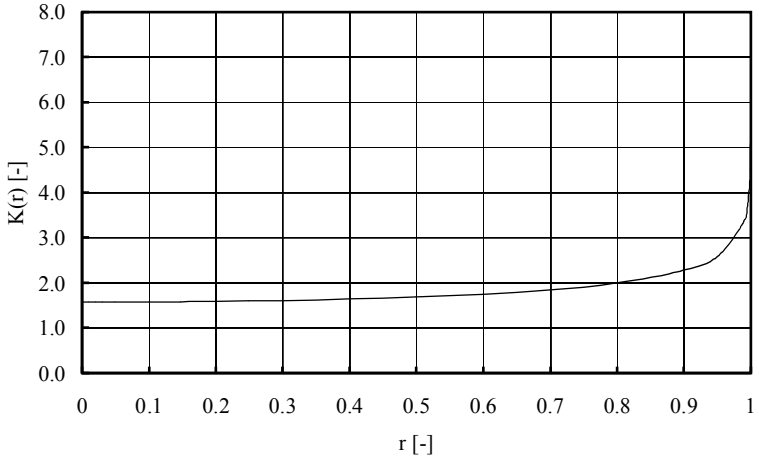

Figure 4.6 The complete elliptic integral *K* versus the ion ratio *r*.

Here we introduce two dimensionless parameters:

$$\Lambda \equiv \frac{d}{D_b}\ [\text{-}] \tag{4.14}$$

and

$$\Pi \equiv \frac{P_s}{RTc^0}\ [\text{-}], \tag{4.15}$$

both of which are functions of the ion ratio r. Λ is a measure of void ratio because the spacing d is linearly related to void ratio as discussed later. Π represents the dimensionless swelling pressure. Dealing with the dimensionless parameters is convenient for later use. The graphs of Λ versus r and Π versus r are plotted in Figure 4.7 and Figure 4.8, respectively.

Combining these two graphs by eliminating r gives the dimensionless plate spacing of Λ versus Π as shown in Figure 4.9. Figure 4.9 tells us the trend of the relationship between Λ and Π.

For water saturated clay, the relationship between water content, which is defined as the weight of water divided by the weight of solid in a soil element, and interparticle spacing is given by

$$w = \frac{S \cdot d}{10^4} \cdot \rho_w\ [\text{-}], \tag{4.16}$$

where w is water content, S the specific surface area of clay in m^2/g, d the half spacing between clay plates expressed in Å, and ρ_w density of water in g/cm^3. On the other hand, from its definition water content is expressed in terms of void ratio as

$$w = \frac{\rho_w}{\rho_s} \cdot e\ [\text{-}], \tag{4.17}$$

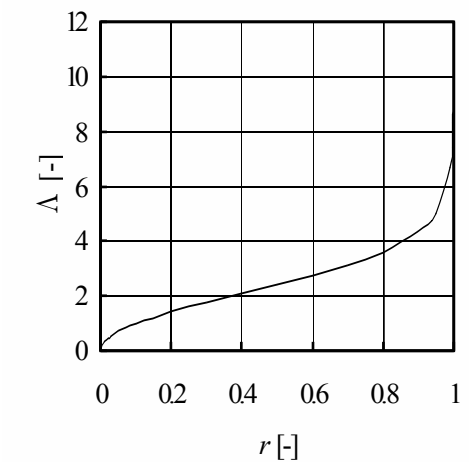

Figure 4.7 Λ **versus** ***r.***

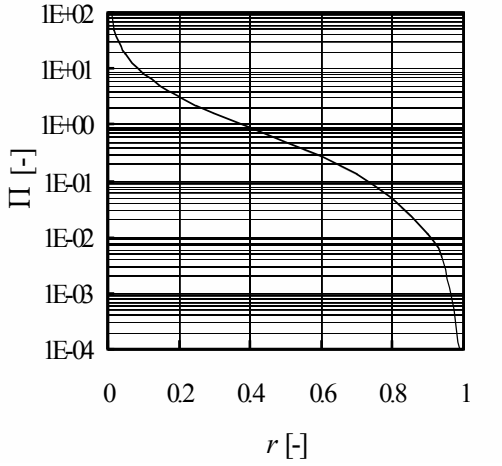

Figure 4.8 Π **versus** ***r.***

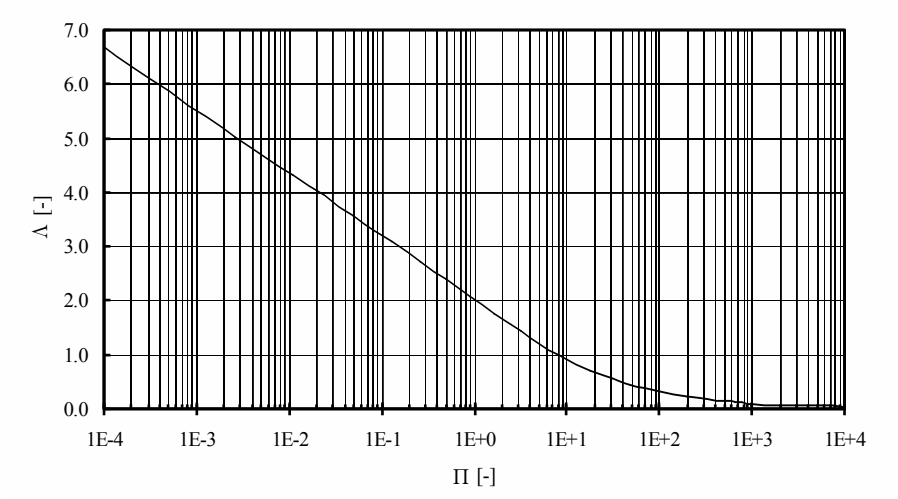

Figure 4.9 Relationship between Λ **and** Π **.**

where ρ_s is density of solid phase in g/cm^3, e void ratio. Thus, equating (4.16) and (4.17) yields the linear relationship between void ratio and spacing,

$$e = \frac{\rho_s \cdot S}{10^4} \cdot d \ [\text{-}]. \tag{4.18}$$

Thus, evaluating the relationship between Λ and Π shows us the trend of void ratio versus swelling pressure. As we see from Figure 4.9 the relationship between void ratio and logarithm of swelling pressure is not linear, which should be contrasted with the linear relationship assumed in the previous report [5].

4.2.3 Numerical Example

A numerical example provides a quantitative illustration of void ratio versus swelling pressure. So here we take a solution of NaCl as an example, which is reasonable because montmorillonites are formed when volcanic ash weathers in marine water. The parameters that must be known to make this calculation are: specific surface area and density of montmorillonite, kind of ions, concentration of ions in the bulk water, and temperature. We calculate the void ratio and the swelling pressure for the following conditions:

Specific surface area of montmorillonite, S = 800 [m^2/g], [13]

Density of montmorillonite, ρ_s = 2.7 [g/cm^3], [13]

Kind of ions, Na^+ and Cl^-

Ion concentration in the bulk water, $c^0 = 10^{-4}$ [M] and10^{-2} [M]

Absolute temperature, $T = 293$ [K]

The following constants are needed:

Boltzmann constant, $k = 1.38 \times 10^{-23}$ [JK^{-1}]

Avogadro's number, $N = 6.02 \times 10^{23}$ [ions/mol]

Electronic charge, $e = 1.602 \times 10^{-19}$ [C]

Dielectric constant of water, $\varepsilon = 7.0834 \times 10^{-10}$ [$C^2J^{-1}m^{-1}$], [13]

With (4.11) the Debye length for the solution of 10^{-4} [M] NaCl is

$$D_b = \sqrt{\frac{7.0834 \times 10^{-12}[C^2J^{-1}m^{-1}] \times 1.38 \times 10^{-23}[JK^{-1}] \times 293[K]}{2 \times 10^{-4}[molL^{-1}] \times 6.02 \times 10^{23}[ions/mol] \times 10^3[L/m^3] \times (1.6 \times 10^{-19}[C])^2 \times 1^2}}$$

$$= 3.05 \times 10^{-8}[m]$$

$$= 305[Å].$$

In the same way for the solution of 10^{-2} [M] NaCl, we get $D_b = 30.5[Å]$.

Then, the void ratio is computed using (4.14) and (4.18). The swelling pressure is determined by (4.15). The resultant curve of void ratio versus swelling pressure is plotted in Figure 4.10 with the ion concentration in the bulk water as a parameter. The range of swelling pressure (10 kPa - 10 Mpa) has been determined referring to the previous report [5]. The range of void ratio (0 - 16) has been selected by the liquid limit of bentonite, which corresponds to a void ratio of about 15 [7]. The two graphs show that the increase in salt concentration causes a decrease in swelling pressure for the same void ratio in the large void ratio region. On the other hand in the small void ratio region the difference of swelling pressure for the same void ratio is small. This can be interpreted by (4.4). In the small void ratio region the particle spacing is small, and then the midplane concentrations of ions are high, which in turn makes the influence of the ion concentrations in the bulk water region in (4.4) negligible. Thus, the difference of swelling pressure for the same void ratio becomes small. In the large void ratio region, on the other hand, the particle spacing is large, where the midplane concentrations of ions becomes lower, which in turn makes the influence of the ion concentrations in the bulk water in (4.4) significant. Thus, the difference of concentration in the bulk water affects swelling pressure for the same void ratio.

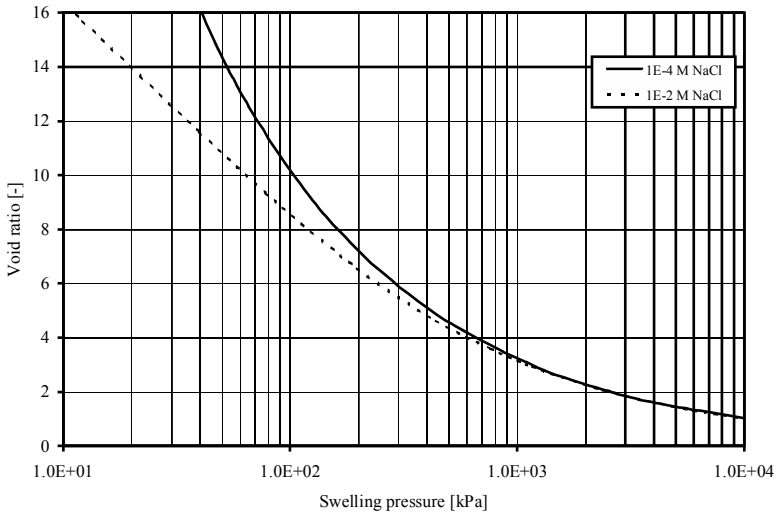

Figure 4.10 Relationship between void ratio and swelling pressure.

4.3 Compressibility

In soil mechanics it is customary to express stress-strain relationship by plotting void ratio versus stress or swelling pressure [14]. The slope of the resulting curve is defined as the coefficient of compressibility a_v:

$$a_v = -\frac{de}{dP_S}. \tag{4.19}$$

From (4.14), (4.15) and (4.18), we have the following linear relationship between de/dP_s and $d\Lambda/d\Pi$:

$$\begin{aligned}\frac{de}{dP_s} &= \frac{d\left(\dfrac{\rho_s \cdot S \cdot D_b \cdot \Lambda}{10^4}\right)}{d\left(RTc^0 \cdot \Pi\right)} \\ &= \frac{D_b[\text{Å}] \cdot \rho_s[\text{g/cm}^3] \cdot S[\text{m}^2/\text{g}]}{10^4 \cdot R\left[\dfrac{\text{L} \cdot \text{atm}}{\text{mol} \cdot \text{K}}\right] \cdot T[\text{K}] \cdot c^0[\text{mol/L}]} \cdot \frac{d\Lambda}{d\Pi} \quad \left[\frac{1}{\text{atm}}\right]\end{aligned}, \tag{4.20}$$

which can be converted to the unit of [1/Pa] with a factor of 1.01×10^5 [Pa/atm].

We find the derivative $d\Lambda/d\Pi$ analytically.

Suppose Λ is a function of Π; then, Λ can be expressed as

$$\Lambda = f\left(\Pi\right). \tag{4.21}$$

On the other hand, both Λ and Π are functions of r; thus,

$$\Lambda = \Lambda(r), 0 < r < 1, \tag{4.22}$$

$$\Pi = \Pi(r), 0 < r < 1. \tag{4.23}$$

Then we must have

$$\Lambda(r) = f\left(\Pi(r)\right), 0 < r < 1. \tag{4.24}$$

By applying the chain rule for differentiation to (4.24)

$$\frac{d\Lambda}{dr} = \frac{d\Lambda}{d\Pi} \cdot \frac{d\Pi}{dr}, 0 < r < 1. \tag{4.25}$$

Solving for $d\Lambda/d\Pi$, we obtain

$$\frac{d\Lambda}{d\Pi} = \frac{\dfrac{d\Lambda}{dr}}{\dfrac{d\Pi}{dr}}, \tag{4.26}$$

The conditions for (4.26) to be valid are as follows. $\Pi = \Pi(r)$ and $\Lambda = \Lambda(r)$ must be differentiable at $r = r_0$, and $f(\Pi)$ must be differentiable at $0 \le r \le R_c$, where r_0 is an arbitrary point in the range $0 < r < 1$.

We have the analytical formulas for the derivatives of Λ and Π with respect to r,

$$\frac{d\Lambda}{dr} = \frac{1}{\sqrt{r}}\left\{\frac{2E\left(r, \dfrac{\pi}{2}\right)}{1 - r^2} - K\left(r, \frac{\pi}{2}\right)\right\}, \ 0 < r < 1, \tag{4.27}$$

where $E\left(r,\frac{\pi}{2}\right)$ is the complete elliptic integral of the second kind, see [16],

$$E\left(r,\frac{\pi}{2}\right)=\int_0^{\pi/2}\left(1-r^2\sin^2\theta\right)^{1/2}\mathrm{d}\theta,\ 0<r<1, \tag{4.28}$$

and also from (4.9) and (4.15)

$$\frac{d\Pi}{dr}=1-\frac{1}{r^2},\ 0<r<1. \tag{4.29}$$

Substituting (4.27) and (4.29) into (4.26) gives

$$\frac{d\Lambda}{d\Pi}=\frac{\frac{1}{\sqrt{r}}\left\{\frac{2E\left(r,\frac{\pi}{2}\right)}{1-r^2}-K\left(r,\frac{\pi}{2}\right)\right\}}{1-\frac{1}{r^2}},\ 0<r<1. \tag{4.30}$$

In Figure 4.11 $-d\Lambda/d\Pi$ is plotted as a function of r.

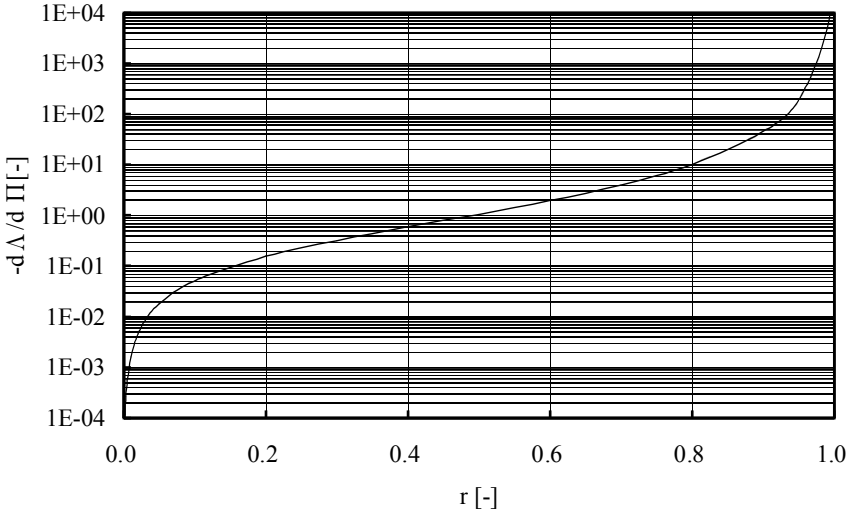

Figure 4.11 $-d\Lambda/d\Pi$ **as a function of r.**

The graph of $-d\Lambda/d\Pi$ versus Π can be obtained by eliminating r between the functions $-d\Lambda/d\Pi$ and $\Pi(r)$. The resultant curve is plotted in Figure 4.12. Also, the graph of $-d\Lambda/d\Pi$ versus Λ obtained in the same way is plotted in Figure 4.13.

Thus, we can calculate the coefficient of compressibility in (4.19) using (4.20) and Figure 4.12 or Figure 4.13. The obtained coefficient of compressibility can be illustrated graphically by drawing a tangent on the figure of void ratio versus swelling pressure. As we see from Figure 4.10, the lower the ion concentration in the bulk water, the steeper is the slope of a tangent, which means that the lower the ion concentration in the bulk water, the more expansive is the bentonite.

In order to obtain the coefficient of compressibility of bentonite, the kinds of ions and their concentrations in the bulk water must be determined in an experiment. The results of this chapter give guidance to experimentalists for the determination of the coefficient of the compressibility.

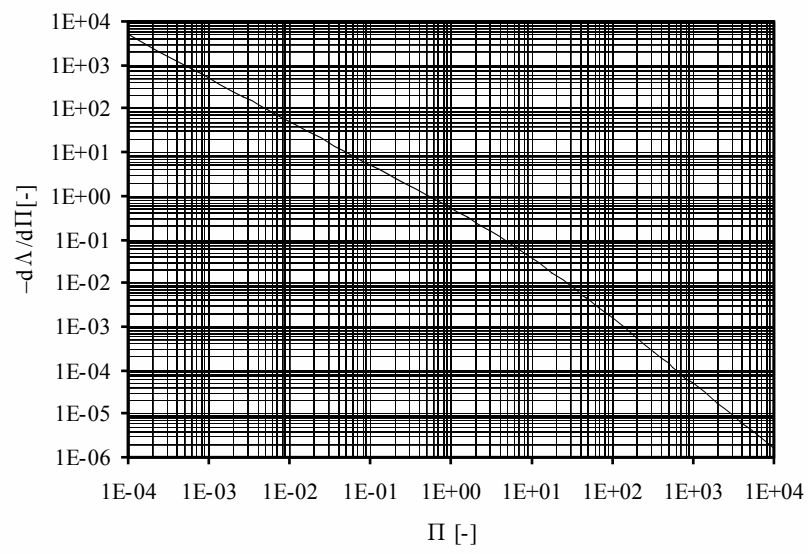

Figure 4.12 $-d\Lambda/d\Pi$ **as a function of** Π .

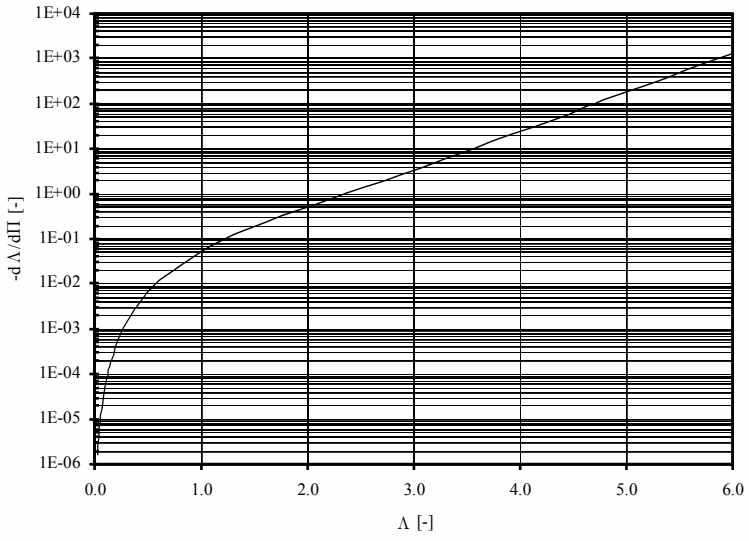

Figure 4.13 $-d\Lambda/d\Pi$ **as a function of** Λ **.**

4.4 Summary

The purpose of this chapter has been to investigate the coefficient of compressibility; namely, the relationship between void ratio and swelling pressure in the swelling of bentonite. The osmotic pressure concept has been applied to the swelling of bentonite by assuming that montmorillonite, the main clay mineral in bentonite, is a plate-shaped clay mineral with its surface negatively charged. Spacing between two particles, and swelling pressure have been derived as a function of ion ratio, which is defined as the ratio of the equilibrium ion concentration in the bulk water to the cation concentration in the midplane between two clay plates. By eliminating the ion ratio between spacing and swelling pressure, the swelling pressure has been related to the spacing, which, in turn, is related linearly to void ratio. The resultant curve of void ratio versus logarithm of swelling pressure is not linear, which is different than the linear relationship assumed in the previous report [5]. In order to obtain the actual curve between void ratio and swelling pressure, the kinds of

ions and their concentrations in the bulk water must be determined in an experiment. The results of this chapter give guidance to experimentalists for the determination of the coefficient of the compressibility.

5. Conclusions

This study has been conducted to refine the study performed by *Ahn, Chambré and Verbeke* on the behavior of bentonite buffer in a geologic repository for high-level wastes [5]. The following refinements have been made:

In Chapter 2, it has been demonstrated that there are several combinations of the diffusion coefficient and the void ratio at the tip giving a good agreement with the experimental curve in contrast with the single combination of the diffusion coefficient and the void ratio at the tip found to fit the experimental result in the previous report [5]. Further experiments for the diffusion coefficient and the void ratio at the tip must be conducted so that unique values can be obtained. Otherwise, the results of matching the experiment are non-unique.

In Chapter 3, a new model, Model 1, to calculate the tip position of expanding bentonite as a function of time has been introduced by Chambré. Model 1 gives the tip position as a function of time without knowing the diffusion coefficient or the void ratio at the tip through the introduction of a single parameter β. With the fitting to the experimental curve in a time range $0 \le t \le 100$ hr, β is fixed at 0.95. Model 1 has an advantage over the previous model at this stage where the available experimental information cannot fix the diffusion coefficient and the void ratio at the tip. However, Model 1 still cannot predict the tip position beyond the time range of the experiment because β depends on the time range in which the experimental data is available.

In Chapter 4, an analysis to obtain the theoretical expression of compressibility of bentonite, one of the three components in the diffusion coefficient, has been made by applying the osmotic pressure concept to the swelling of bentonite. The obtained curve of void ratio versus logarithm of swelling pressure is not linear, which differs from the linear relationship assumed in the previous report [5]. When the equilibrium ion concentrations in the bulk water is given by experimental measurements, the compressibility of bentonite can be calculated using the method described in this report. The basic assumption made to apply the osmotic pressure concept is that all the tabular clay particles are oriented in a parallel fashion. In reality, however, there will be differently oriented particle groups with dead space in between. This can be taken into consideration by reducing the assumed specific surface area value, which is generally taken as 800 m^2/g for oriented dispersed sodium montmorillonite particles. One third of the value for oriented particles, i.e. about 270 m^2/g, is said to be plausible [15].

Prof. Chambré has told me about a rule of conduct, that the process in Science is, in a phrase of Prof. Morris Cohen [17], “A process of continual self correction”.

6. References

[1] J. Ahn, P. L. Chambré, B. Light, D. Roberts, and J. Verbeke, *Radionuclide Transport in Disturbed Zone Between Engineered and Natural Barriers of Deep Geologic Disposal of High-Level Radioactive Wastes*, UCB-NE-4217, 1996.

[2] R. Push, *Stability of Bentonite Gels in Crystalline Rock — Physical Aspects*, SKBF/KBS Technical Report 83-04, 1983.

[3] T. Kanno and H. Wakamatsu, *Experimental Study on Bentonite Gel Migration from a Deposition Hole*, Proc. 3rd Int. Conf. Nuclear Fuel Reprocessing and Waste Management (RECOD '91), 1991.

[4] Power reactor and Nuclear Fuel Development Corporation, *Evaluation of extrusion of bentonite buffer (I)*, PNC TN8410 97-313, 1997.

[5] J. Ahn, P. L. Chambré and J. Verbeke, *Long-term Behavior of Bentonite Buffer in a Geologic Repository for High-level Wastes*, UCB-NE-4222, 1999.

[6] K. Terzaghi, R. B. Peck, G. Mesri, *Soil Mechanics in Engineering Practice, 3rd ed.*, Wiley-Interscience, 1996.

[7] R. N. Yong and B. P. Warkentin, *Soil Properties and Behaviour*, Elsevier Scientific Publishing Co., 1975.

[8] P. L. Chambré, *Chapters 3 and 4 of this report are part of a manuscript to be published.*

[9] A. Jeffrey, *Basic Mathematics for Engineers and Technologists*, Nelson, 1974.

[10] B. M. Mahan and R. J. Myers, *University Chemistry, fourth ed.*, Benjamin/Cummings, 1987.

[11] G. M. Barrow, *Physical Chemistry, second ed.*, McGraw-Hill, 1966.

[12] H. v. Olphen, *An Introduction to Clay Colloid Chemistry*, Wiley-Interscience, 1963.

[13] J. K. Mitchell, *Fundamentals of Soil Behavior*, second ed., Wiley-Interscience, 1993.

[14] T. W. Lambe and R. V. Whitman, *Soil Mechanics*, Wiley, New York, 1969.

[15] R. Pusch, *Self-injection of highly compacted bentonite into rock joints*, KBS Teknisk Rapport 73, 1978.

[16] M. Abramowitz and I. A. Stegun, *Handbook of Mathematical Functions*, Dover Publications, Inc., 1970.

[17] M. Cohen and E. Nagel, *An Introduction to Logic and the Scientific Method*, Hartcourt, Brace, New York, Page 395, 1934.